Journal of Raman Spectroscopy

WILEY

Journal of RAMAN SPECTROSCOPY

RESEARCH ARTICLE OPEN ACCESS

Dolomite and Mg Calcite as Mineral Thermometers in Mortar Binders. A High Resolution Raman Spectroscopic Study

Moritz T. Zöllner[1,2] | Petra Dariz[3,4] | Jens Riedel[1] | Thomas Schmid[1,4,5]

[1]Division of Instrumental Analytics, Federal Institute for Materials Research and Testing (BAM), Berlin, Germany | [2]Department of Chemistry, Humboldt-Universität zu Berlin, Berlin, Germany | [3]Conservation-Restoration, Bern University of the Arts, Bern University of Applied Sciences, Bern, Switzerland | [4]Heritagelab Foundation, Bolzano, Italy | [5]School of Analytical Sciences Adlershof (SALSA), Humboldt-Universität zu Berlin, Berlin, Germany

Correspondence: Petra Dariz (petra.dariz@gmail.com) | Jens Riedel (jens.riedel@bam.de)

Received: 26 February 2025 | **Revised:** 18 March 2025 | **Accepted:** 24 March 2025

Funding: We gratefully acknowledge funding of this research by the Deutsche Forschungsgemeinschaft DFG (Project no. 458702855) and the Interreg VI-A Italy-Austria program 2021-2027 (Project no. ITAT-11-027 SaltAR).

Keywords: dolomite | high-fired gypsum mortar | Mg calcite | Raman imaging

ABSTRACT

This paper suggests the use of high-resolution Raman scattering bands of Mg—Ca carbonates as posteriori thermometer minerals in archaeometric studies. Therefore, the thermal behavior of two dolomite samples and the hydration and carbonation reaction in air of the decomposition products were investigated by Raman microspectroscopy. The increase in the calcination temperature resulted in the formation of – Raman silent MgO and – inert Mg calcite at 700°C–750°C. In contrast, the decarbonation, hydration, and recarbonation of sample material exposed to 750°C–900°C in a muffle furnace led to the appearance of Mg-free calcite. High spectral resolution Raman spectroscopy enabled a spectral distinction between these two groups due to differences in the band parameters (peak position, bandwidth) of the vibrational (v_1, v_4, L) modes of calcite. In combination with Raman microspectroscopic mapping, this spectral information represents a new approach for the estimation of burning temperatures of medieval high-fired gypsum mortars via natural dolomite impurities. Thus, the results of this work highlight the importance and potential of Raman microspectroscopy as a thermometric tool for elucidating the thermal history of anthropogenic fired materials, with potential applications for archaeometry and art technology, as well as for quality controls in the frame of the production of mineral mortar binders and ceramics or bricks, respectively.

1 | Introduction

In correlation with local geological circumstances, dolomite rock ($CaMg(CO_3)_2$) or dolomitic lime was traditionally used just as limestone (calcite $CaCO_3$) as raw material for the production of mortars and plasters. The thermal decomposition of dolomite ($CaMg(CO_3)_2 \rightarrow CaO + MgO + 2CO_2$) proceeds depending on the burning regime or experimental conditions, respectively, which explains the spread of temperature specifications available in the literature. Under high CO_2 partial pressure in the calcination atmosphere of a traditional lime kiln, the dissociation is reported to proceed along a two-step mechanism: Firing at temperatures between 500°C and 700°C results in the formation of periclase (MgO) and quicklime (CaO), followed by the immediate recarbonation of the latter. As the temperature is further increased to 700°C–900°C, the newly formed $CaCO_3$ is converted into CaO. Slaking of the calcinated dolomite yields brucite ($Mg(OH)_2$) and portlandite ($Ca(OH)_2$), while the carbonation reaction closes the

lime cycle by the non-contemporaneous and independent crystallization of magnesite ($MgCO_3$), via hydrous magnesium carbonate and amorphous phases, and of the $CaCO_3$ polymorphs aragonite and calcite [1–9].

In the last decennia, micro-Raman spectroscopy has been increasingly applied for the analysis of pyrometamorphism products, often present only in trace amounts, by combining high spatial resolution with the capability to detect minor chemical–structural changes within the crystal lattice in a highly detailed Raman microspectroscopic mapping. This method has been successfully applied, e.g., for the characterization of not hydrated clinker phases in 19th century cement mortars and for studying the sintering reactions in ceramics and cementitious materials [10–15]. Due to a significant narrowing of the Raman bands in the range of 400°C–900°C, the determination of Raman spectral bandwidths (full width at half maximum, FWHM) of pyrogenic anhydrite allowed the estimation of the burning temperature of high-fired gypsum mortars used as masonry and joint mortars or for stuccowork in Central Europe in the Early and High Middle Ages [16–21]. As for carbonate minerals, Raman micro-spectroscopy and spectroscopic mapping have been used for profiling the carbonation depth in lime mortars [22, 23] and for the characterization of amorphous and crystalline calcium carbonate in biogenic limestone samples [24–26]. More recently, the exact spectral peak positions and FWHM of Raman bands were shown to reflect the degree of crystallinity and atomic disorder in bulk samples and thin sections. This paved the way to a spectroscopic discrimination between geogenic and anthropogenic calcites [27, 28].

Despite these promising research activities, comprehensive and thorough Raman microspectroscopic mappings in combination with band position and bandwidth analyses are still scarce. Particularly, dolomite with its multiple transformation steps (as shown with XRD, IR-Spectroscopy, and electron microprobe analysis [6–8, 29–31]) bears great potential for the reconstruction of the thermal history of anthropogenic fired materials such as mortars or ceramic. In this work, the thermal breakdown of natural dolomite in a muffle furnace and the subsequent hydration and carbonation reaction upon air exposure of the decomposition products are experimentally studied with high-spectral resolution Raman spectroscopy. The experimental findings are applied on a reenacted high-fired gypsum mortar containing dolomite as geologically related natural impurity using Raman microspectroscopic mapping. The thermally stressed dolomites serve as additional temperature indicators complementing the above-mentioned spectral and thermal information gathered on the basis of not hydrated pyrogenic anhydrites typically preserved in the binder matrix of such mortars. The calcination at temperatures of up to 900°C results in an assemblage of calcium sulfate phases dehydrated to different degrees and partly thermally damaged accessory minerals of the raw gypsum (carbonates, phyllosilicates, etc.)—the only source to the lost medieval technological know-how.

2 | Experimental

2.1 | Samples

Two natural dolomite samples were used for the thermal experiments: Sample DPK (abbrev. for Dolomite Powder Kremer) was purchased as a powder from Kremer Pigmente GmbH & Co. KG in Aichstetten, Germany, whereas the rock sample DRR (abbrev. for Dolomite Rock Rudelswalde, quarry location in Germany) was provided by the Museum für Naturkunde Berlin – Leibniz Institute for Evolution and Biodiversity Science. Sample DRR was manually powdered with an agate mortar prior to the thermal experiments. Upon grinding, it exhibits a yellowish-brown color due to impurities of Fe_2O_3 and MnO (XRF data in Table 1). The white sample DPK is characterized by a high purity of 99% $CaMg(CO_3)_2$ with only minor amounts of Fe_2O_3 [32]. Raman analysis of the dolomite ν_1-band showed FWHM values of $5.5 \pm 0.2\,cm^{-1}$ and $5.3 \pm 0.7\,cm^{-1}$ in the samples DPK and DRR, respectively, indicating a similar degree of crystallinity before thermal treatment.

The findings from the thermal experiments with dolomite were compared with observations made on a real-life mortar sample containing dolomite impurities in a proof-of-concept study. Microscopic Raman analysis was applied on individual grains of a high-fired gypsum mortar prepared in 2012 according to traditional procedures at the Ziegelei Technisches Denkmal Hundisburg e.V. in Haldensleben, Germany [33]. This reenacted binder type was named KeuperM after gypsum deposits of the Keuper period quarried at Bad Windsheim, Germany. Dolomite, dolomitic marl, celestine, quartz, and feldspar are confirmed as minor constituents of the raw material. According to the manufacturer, firing temperatures of up to T = 900°C were used in producing the high-fired gypsum [33]. To make accessible a representative cross section, the mortar sample was embedded in epoxy resin (Huntsman Araldite® 2020) and polished to thin sections (30 μm thickness). A polarizing light microscope (Zeiss Axio Scope.A1 MAT equipped with AxioCam MRc) was used with reflected light and transmitted light to assign study segments suitable for Raman analysis.

TABLE 1 | Oxide composition (wt %) of the two natural dolomite samples used for the thermal experiments in this work. Wavelength dispersive X-Ray Fluorescence (WDXRF) measurements were conducted with a MagiX Pro from PANalytical equipped with a water-cooled 4-kW Rh tube. Data quantification was done using the semi-quantitative measurement program "Omnian" (n.d.: not detected).

Oxide wt %	Dolomite Powder Kremer (DPK)	Dolomite Rock Rudelswalde (DRR)
SiO_2	0.39	0.45
Al2O3	0.07	0.19
Fe2O3	0.21	0.6
MnO	n.d.	0.41
MgO	18.06	17.61
CaO	39.81	39.12
Na2O	n.d.	0.14
K2O	0.03	0.03
Total	58.57	58.55

2.2 | Dolomite Decomposition and Recarbonation

Two grams each of dolomite powder from samples DPK and DRR were weighed into corundum crucibles and calcinated for 2 h in a laboratory muffle furnace (LT9/13/P320 Nabertherm, Lilienthal, Germany) at the defined burning temperatures T_{burn} = 500, 600, 700, 750, 800, 850, and 900°C. After cooling down to room temperature (RT), a part of the burnt powders was mixed with 5 mL water in a glass cylinder with a magnetic stirrer, after which 0.2 mL of the suspension was pipetted onto a microscope slide and exposed to the CO_2 in ambient air.

2.3 | Raman Spectroscopy

Raman spectroscopic measurements were conducted on a LabRAM HR800 instrument (Horiba Jobin Yvon) coupled to a BX41 microscope (Olympus) with a 50×/N.A. = 0.55 long working distance objective and a charge coupled device (CCD) detector (Symphony, Horiba Jobin Yvon). The second harmonic of a continuous Nd:YAG laser output at λ = 532 nm was used as the probe laser beam for all measurements. To minimize laser-induced peak broadenings or shifts (see Figure S1 in Supporting Information), as well as laser-induced sample deterioration, the laser intensity was carefully adjusted to a power between 1 and 16 mW on the sample surface. The exact value of attenuation was achieved using the combination of several neutral density filters and determined by monitoring the spectral broadening online. The width of the spectrometer entrance slit was 100 μm and the diameter of the confocal pinhole was 1000 μm. An 1800 mm^{-1} grating was used for diffraction, resulting in a natural spectral resolution of approx. 0.45 cm^{-1} per CCD pixel at 1100 cm^{-1}. The spectral coverage of the CCD detector, i.e., the width of the spectral window that can be detected with a specific grating inclination, is approx. 450–500 cm^{-1} with the incident laser wavelength at 532 nm. The spectrometer is equipped with a movable grating system that allows the adjustment of the angle of diffraction to measure at different wavelengths. Due to non-uniform movements, hysteresis, and necessary leeway of the mechanical system, systematic peak position shifts of few pixels are observed on the same Raman band depending on the absolute spectral window, i.e., the rotation angle of the grating [34, 35]. To determine absolute spectral positions even below this inherent uncertainty, careful internal calibration of the peak positions with atomic emission lines is preferable, e.g., using a neon or mercury-argon lamp, but parallel acquisition of emission lines at the sample position is often impractical and requires a set-up with an external or internal calibration lamp. In this study, the spectrograph wavelength position (monikered "Spectro" in the Horiba LabSpec6 software suite) was manually set to regions around the central wavenumbers of 350, 700, and 1100 cm^{-1} for the measurement of the carbonate *L*- (librational mode), ν_4- (in-plane bending), and ν_1- (symmetric stretching) bands, respectively, to minimize the systematic deviation introduced by software-controlled selection of the detection windows and thus improve reproducibility. Also, the spectral range function provided by the LabSpec6 software, which combines multiple measurement windows within a given spectral range into one continuous spectrum was avoided, when possible, since it results in a loss of raw spectral data due to limited control over the preprocessing parameters.

Typical acquisition times for single measurements were 10–30 s (5 × 2 s/6 × 5 s), depending on the signal-noise ratio. To ensure better statistics, a minimum of three sets of Raman maps were acquired at different locations on the sample surface, each with a dimension of 4 × 4 pixels with 100 μm × 100 μm step sizes, leading to a sample size of at least 48 spectra per measurement campaign. These non-spatially resolved Raman measurements were performed on the calcinated dolomite samples before hydration as well as after 1 day of recarbonation in ambient air. Further Raman measurements were conducted over the course of four months to observe chemical–structural changes during the continuous recarbonation process. Larger Raman maps (8000–20,000 px, 2 μm step sizes, min. 2 × 1 s per spectrum) were used for the analysis of the thin sections of the mortar sample KeuperM at specific areas that were selected after analysis with the polarization microscope.

Peak fitting was applied on the Raman spectroscopic data to determine peak positions and band widths out of the superimposed individual features in the spectra. Briefly, the peak fitting workflow is oriented on similar routines used by other authors [17, 25, 36]. In this work, the data processing pipeline including preprocessing, fitting, and value extraction was highly automated using Python scripts, including the open access package lmfit for non-linear least-squares minimization and curve fitting [37]. In the preprocessing steps, the raw Raman spectra were masked to a narrower spectral range to increase the impact of the bands of interest onto the fitting residuals. Peak intensities were normalized, and peak-fitted using the superposition of a linear baseline and singular or multiple Pseudo-Voigt peaks. Boundaries of the fitting parameters were defined individually for each Raman mode to restrict and optimize the fitting procedure. Examples of fitted spectra are shown in Figure S2 of the Supporting Information.

3 | Results and Discussion

3.1 | Calcination of Dolomite: ν_1-Mode

After heating up to T_{burn} = 500°C, the observed Raman spectra of both dolomite samples resemble the original spectra without heating. After calcination at T_{burn} = 600°C, a faint shoulder around 1089 cm^{-1} becomes visible (Figure 1A). The intensity of this shoulder increased upon further heating to 700°C, leading to a distinct separate peak. The high spectral resolution of our setup allows for a global fit of the spectral region as a superposition of two individual spectral bands, one centered around 1098 cm^{-1} for dolomite and one around 1089 cm^{-1}. Comparison with the literature enables an assignment of the latter peak as a contribution from Mg calcite [38, 39]. The peak integrals of the fit result can be used for a quantitative characterization of the two contributions. Accordingly, dolomite was still predominant in the Raman spectra of sample DPK after calcination at 700°C. After heating to the same temperature, the sample DRR was already dominated by the Mg calcite band with only minor contribution of residual dolomite.

Some traces of calcite with band positions around 1086 cm^{-1} and lower FWHM values of 2–3.5 cm^{-1} were also found in the DPK sample calcinated at 700°C. These values matched those of the calcite impurities found in sample DPK at room temperature and therefore suggested the continued presence of uncalcinated,

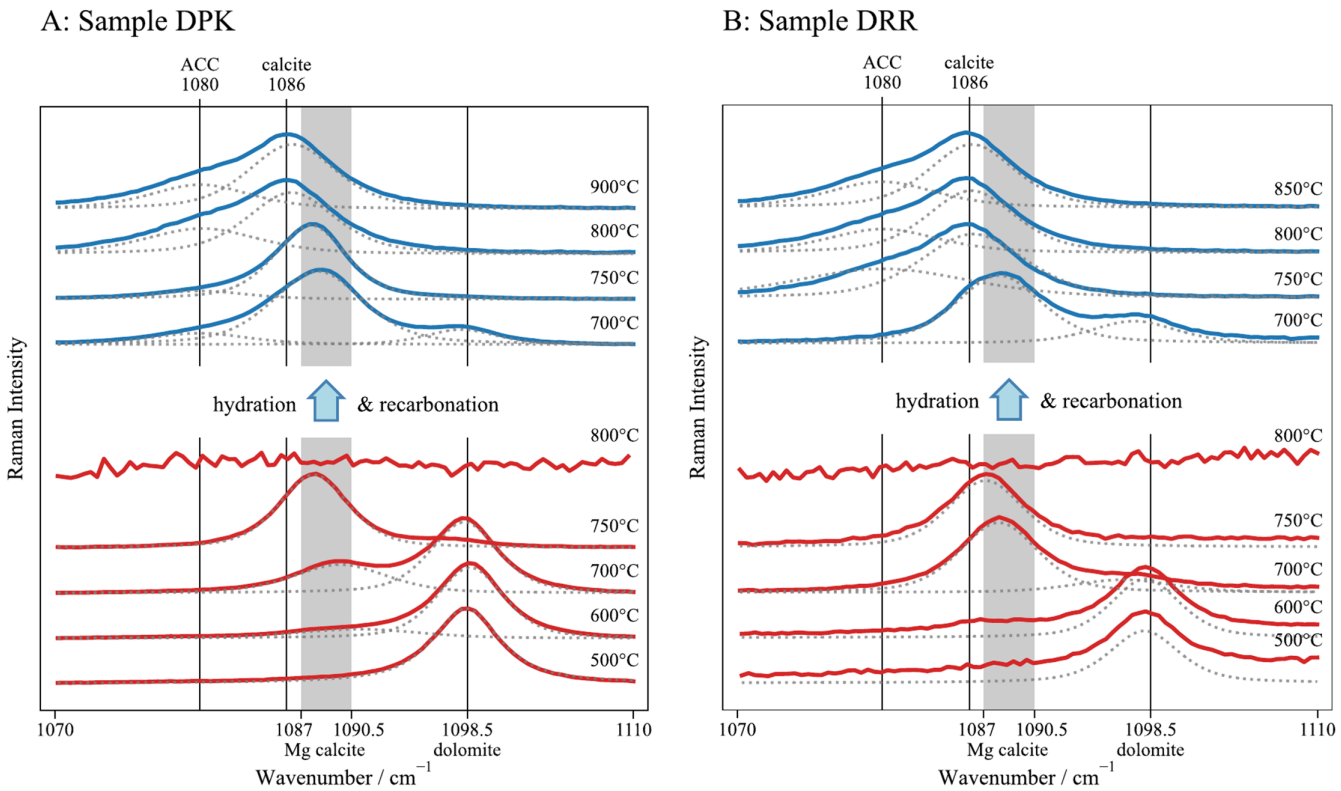

FIGURE 1 | Raman spectra of ν_1-bands of carbonates measured at room temperature after calcination at different burning temperatures T_{burn} (red) and after subsequent hydration and recarbonation for 1 day (blue) for dolomite samples DPK (A) and DRR (B). The spectra are normalized, averaged over 16 measurements, and vertically offset for clarity. Deconvoluted bands from peak fitting are shown under each spectrum in grey. Peak position values of relevant carbonates are highlighted with vertical lines and boxes.

primary calcite at 700°C. Overall, the amount of calcite was only minor compared to the amount of Mg calcite at 700°C in both dolomite samples.

After calcination at 750°C, the band intensities of dolomite decreased strongly in sample DPK, and the ν_1-band of Mg calcite became the predominant spectral feature. Comparison of the ν_1-band of Mg calcite showed, that the mean peak position shifted slightly towards lower wavenumbers from approx. 1089.6 cm^{-1} at 700°C to approx. 1087.8 cm^{-1} at 750°C in sample DPK, and from 1088.2 cm^{-1} at 700°C to 1087.2 cm^{-1} at 750°C for sample DRR (Table 2).

A proportional spectral shift of peak position as well as peak broadening of the Raman bands with increasing Mg content was previously described for various carbonates [38, 40, 41]. This shift is explained by the decrease of interatomic distances in the crystal lattice due to the substitution of the larger Ca^{2+} ions by the smaller Mg^{2+} ions. The shorter Mg—O bond is stronger than the longer Ca—O bond and hence induces a weakening with a corresponding red shift in the vibrational modes of the C—O bonds of the carbonate [38, 41–43]. Raman analyses on synthetic and biogenic Mg calcites also showed proportionally increasing peak positions and bands widths of all vibrational modes with increasing Mg concentrations [38, 39]. The studies reported comparably high peak position values of 284–286 cm^{-1} for the L-mode, 714–716 cm^{-1} for the ν_4-mode, and 1087–1088 cm^{-1} for the ν_1-mode, which corresponded to high-Mg calcites with concentrations of approx. 8–15 mol% $MgCO_3$. Low-Mg calcites (0–4 mol% $MgCO_3$) on the other hand usually showed lower peak position values of 280–281 cm^{-1}, 711–712 cm^{-1}, and 1085–1086 cm^{-1} for the L-, ν_4-, and ν_1-bands, respectively. The decrease of peak position and FWHM values observed in the spectra of samples calcinated between 700°C and 750°C was therefore an indication of decrease of Mg concentration, though the values were still well within the boundaries of high-Mg calcite.

After heating above 800°C, the Mg calcite bands disappeared in the Raman spectra of both samples while several weaker signals of portlandite around 360 cm^{-1} and amorphous calcium carbonate (ACC) at 1080 cm^{-1} occurred (Figure S3 in Supporting Information), suggesting the complete breakdown of dolomite and Mg calcite to CaO and MgO, which are known to be Raman-inactive [44–46]. The spontaneous formation of portlandite and ACC directly after calcination is a frequently observed phenomenon, as freshly produced CaO reacts with the water vapor and CO_2 of the ambient air. The metastable ACC subsequently transforms into more stable, crystalline calcium carbonate polymorphs via dissolution–precipitation processes as the carbonation reaction continues [47–50].

3.2 | Hydration and Recarbonation of Calcinated Dolomite: ν_1-Mode

While directly after calcination the amount of observed ACC was low, an increase in ACC formation was detected after one

TABLE 2 | Raman peak positions and band widths of calcium carbonate bands in thermally treated dolomite samples DPK and DRR after calcination (top two rows), and after hydration and recarbonation for 1 day and 130 days. Mean and standard deviation derived from 48 spectra at each burning temperature T_{burn}.

T_{burn}	Position (DPK)	FWHM (DPK)	Position (DRR)	FWHM (DRR)	Position (DPK)	FWHM (DPK)	Position (DRR)	FWHM (DRR)	Position (DPK)	FWHM (DPK)	Position (DRR)	FWHM (DRR)
[°C]	ν_1 [cm^{-1}]	ν_1 [cm^{-1}]	ν_1 [cm^{-1}]	ν_1 [cm^{-1}]	ν_4 [cm^{-1}]	ν_4 [cm^{-1}]	ν_4 [cm^{-1}]	ν_4 [cm^{-1}]	L [cm^{-1}]	L [cm^{-1}]	L [cm^{-1}]	L [cm^{-1}]
700	1089.6 ± 0.3	7.6 ± 0.4	1088.2 ± 0.2	6.3 ± 0.5	715.1 ± 1.0	12.0 ± 2.0	713.7 ± 0.8	9.1 ± 1.6	285.5 ± 0.4	17.3 ± 0.8	282.2 ± 1.0	18.5 ± 1.6
750	1087.8 ± 0.3	5.5 ± 0.3	1087.2 ± 0.3	5.9 ± 0.6	713.3 ± 0.3	7.2 ± 0.7	713.0 ± 0.7	7.5 ± 1.5	282.7 ± 0.5	15.1 ± 0.6	280.0 ± 1.6	17.8 ± 2.3
recarb. 1d												
700	1088.3 ± 0.2	6.9 ± 0.3	1087.9 ± 0.6	6.7 ± 0.6	713.6 ± 0.3	9.6 ± 0.5	713.1 ± 0.8	8.1 ± 1.6	283.1 ± 0.5	20.9 ± 1.6	282.0 ± 0.9	17.6 ± 1.2
750	1087.7 ± 0.1	5.6 ± 0.1	1086.3 ± 0.4	6.7 ± 0.5	713.3 ± 0.1	8.1 ± 0.3	712.1 ± 0.4	10.9 ± 1.4	282.4 ± 0.2	16.7 ± 0.6	277.4 ± 0.9	24.5 ± 1.1
800	1086.3 ± 0.2	6.9 ± 0.4	1086.1 ± 0.2	6.7 ± 0.4	712.1 ± 0.2	11.0 ± 0.8	712.0 ± 0.2	11.4 ± 0.7	278.5 ± 0.2	24.0 ± 0.6	276.8 ± 0.6	25.8 ± 1.2
900/850	1086.4 ± 0.1	6.9 ± 0.4	1086.2 ± 0.1	6.8 ± 0.4	712.1 ± 0.3	11.3 ± 0.9	712.1 ± 0.2	10.7 ± 0.7	278.5 ± 0.1	23.8 ± 0.7	277.3 ± 0.3	25.1 ± 0.6
recarb. 130d												
700	1087.8 ± 0.3	7.0 ± 0.5	1087.4 ± 0.6	6.3 ± 0.7	713.4 ± 0.3	9.3 ± 0.7	713.0 ± 0.9	7.8 ± 1.7	282.9 ± 0.5	20.0 ± 1.2	282.3 ± 0.8	16.8 ± 1.1
750	1087.5 ± 0.1	5.7 ± 0.2	1085.6 ± 0.3	5.7 ± 0.6	713.5 ± 0.1	8.0 ± 0.3	711.6 ± 0.3	9.7 ± 0.8	282.3 ± 0.2	16.5 ± 0.6	277.9 ± 0.4	21.9 ± 0.7
800	1085.9 ± 0.2	6.1 ± 0.4	1085.4 ± 0.1	5.6 ± 0.5	712.2 ± 0.3	9.8 ± 0.9	711.4 ± 0.3	9.7 ± 1.0	278.7 ± 0.2	21.8 ± 0.6	277.3 ± 0.3	22.7 ± 0.7
900/850	1086.0 ± 0.1	6.1 ± 0.3	1085.4 ± 0.1	5.6 ± 0.5	712.1 ± 0.5	9.8 ± 1.1	711.5 ± 0.2	9.5 ± 1.0	278.7 ± 0.2	21.8 ± 0.6	277.5 ± 0.2	22.4 ± 0.6

day of hydration and recarbonation of the dolomite samples, indicated by a broad shoulder around 1080 cm^{-1} that emerged in the samples priorly exposed to burning temperatures above 800°C for DPK and above 750°C for DRR (Figure 1, blue curves). As discussed in the previous section, this ACC is not thermodynamically stable long-term and transforms into stable calcite as the carbonation process continues. Indeed, further exposure of the recarbonated samples to air over four months under open laboratory conditions resulted in a relative decrease in the ACC-to-calcite intensity, and the continuous decrease of the calcite ν_1-band width reflects the increase of crystallinity (Table 2 and Figure S4 in Supporting Information). Prolonged stability of ACC during precipitation of calcium carbonates under conditions of Mg supersaturation and subsequent crystallization of high-Mg calcite has been reported [51–53]. However, such high Mg/Ca ratios are not expected here in the calcinated dolomite samples. Moreover, the low Raman peak position values around 1080 cm^{-1} indicate low Mg content in ACC [41]. ACC with low Mg content is expected to transform into low-Mg calcite [52], which is also observed in the samples aged for approx. four months.

Most of the recarbonated samples which were treated at T_{burn} = 700°C–750°C showed similar mean peak position values around 1087–1088 cm^{-1}, comparable to the values obtained from calcinated samples. A decrease of the Raman peak positions to 1085°C1086 cm^{-1} was apparent in the recarbonated samples treated above 800°C, except for sample DRR prepared at 750°C, which already exhibited a decrease of the Raman peak position to 1085.6 cm^{-1}. These results strongly suggest that the secondary calcite formed from CaO after hydration and recarbonation is depleted in its Mg content. In case of DPK, this low-Mg or Mg-free calcite was predominant in the recarbonated samples heated at 800°C and above, while the low-Mg calcite already dominated the spectra above 750°C in the DRR samples. The earlier appearance of low-Mg calcite in the latter sample indicated that a significant amount of Mg calcite had already been calcinated to CaO at 750°C. Several factors may contribute to the different behaviors during the thermal decomposition of the dolomite samples. Particle sizes and specific surface areas of dolomite affect the timing of the thermally induced transformations and intense mechanical grinding can lead to the formation of calcite and periclase already at 500°C–600°C [54–56]. Impurities such as inorganic salts and metal oxides may also reduce the decomposition temperature [30, 56]. The latter factor may have contributed to a certain degree here, since sample DRR included slightly higher amounts of Fe and Mn in the raw material. On the other hand, other authors indicate that the elemental composition had no significant effect on the overall thermal behavior of dolomite [2].

Overall, the observed FWHM values of the carbonate ν_1-band of Mg calcite and of the recarbonated calcite ranged around 5.5–6 cm^{-1}. Similarly, high values are reported for reformed, anthropogenic calcites, while significantly narrower Raman bands with widths of approx. 2–4 cm^{-1} are typical for primary, geogenic calcites [27, 28]. Slightly higher FWHM values around 7 cm^{-1} in samples calcinated at 700°C are most likely artifacts from poorer fit results, caused by the overall low band intensity and interference from the dominant neighboring dolomite band. For comparison, Raman band parameters of different geogenic samples are given in the Supporting Information (Table S1).

3.3 | Comparison With Raman Peak Position of *L*- and ν_4-Modes

Similar trends and changes in the Raman signals can be observed in the carbonate ν_4- (Figure 2) and *L*-bands (Figure 3) at smaller wavenumbers as well. Comparison of the different Raman modes showed an overall red shift of all calcite bands to lower wavenumbers with increasing temperatures. For a comprehensive overview of the spectral behavior, all samples are plotted in two dimensional spectral plots (Figure 4), in which the graph is spun up by two axes representing the spectral position of the two central peaks of two respective bands. Two clusters emerged when plotting the peak position values of both modes in this biaxial fashion. One group clusters around overall higher band peak values of calcites and can be assigned to sample DPK heated at 700°C and 750°C, as well as sample DRR heated at 700°C. The second group generally exhibits lower band values of calcites and consisted of all other dolomite samples, which were calcinated beyond 800°C for DPK and beyond 750°C for DRR. The differences in band positions of these two clusters are especially pronounced in the plots spun up by the ν_1- and ν_4-modes against the *L*-mode. The two intramolecular vibration bands showed comparably moderate peak shifts of 2–5 cm^{-1}, while a peak shift of up to 12 cm^{-1} could be observed for the intermolecular *L*-mode. This different response on cation exchange reflects the expected change of intermolecular vs. intramolecular atom–atom distance upon intercalation.

The larger peak positions values of the first group were attributed to the higher residual Mg content in the crystal lattice of calcite that was directly formed during the decomposition of dolomite at 700–750 °C. Several authors reported the conversion of dolomite directly into CaO, MgO, and CO_2 at this temperature range and an immediate carbonation of CaO to $CaCO_3$, while MgO remains unreacted [1, 57, 58]. Rodriguez-Navarro et al. argue the initially formed CaO and MgO to be solid-solutions with considerable amounts of Mg or Ca, respectively, which results to the non-pure CaO subsequently reforming as Mg calcite. Further calcination at higher temperatures then leads to the dissociation of Mg from Mg calcite and decomposition into pure CaO [1]. This formation of solid solutions of CaO and MgO could neither be confirmed nor disproven with the analytical approach of our study. However, our Raman spectroscopic results, under the given firing conditions, corroborate the presence of a two-step decomposition of dolomite with Mg calcite forming in a transitional step before further calcinating to CaO in a second step at elevated temperatures.

The lower band position values of the second group suggest that Mg was not re-incorporated into the reformed calcite after hydration and recarbonation. Furthermore, the significantly decreased peak positions of the *L*-band with values below 280 cm^{-1} indicate a high structural disorder of the reformed calcite. Calandra et al. and Toffolo et al. utilized this shift of the *L*-mode to distinguish between geogenic and anthropogenic calcites [27, 28]. The results here in this work demonstrate that the same

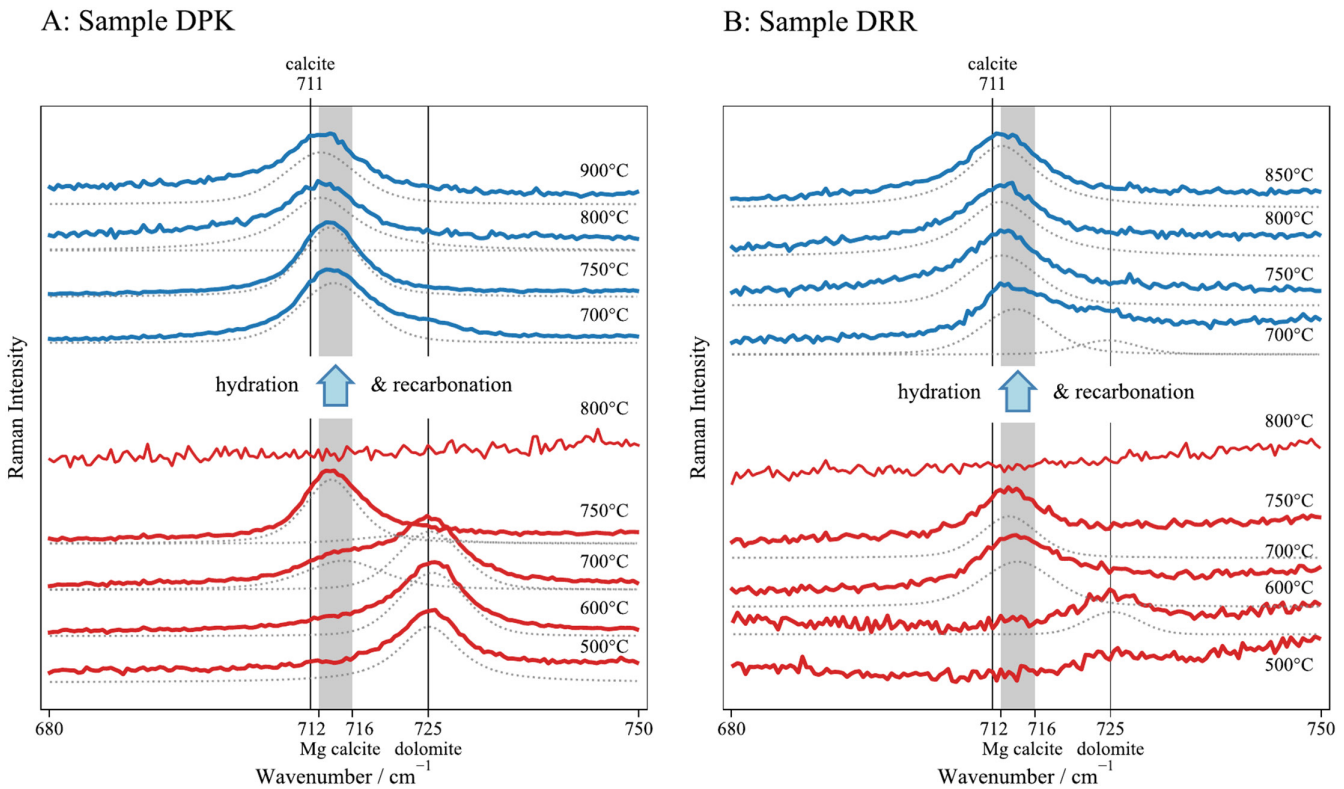

FIGURE 2 | Raman spectra of v_4-bands of carbonates measured at room temperature after calcination at different burning temperatures T_{burn} (red) and after subsequent hydration and recarbonation for 1 day (blue) for dolomite samples DPK (A) and DRR (B).

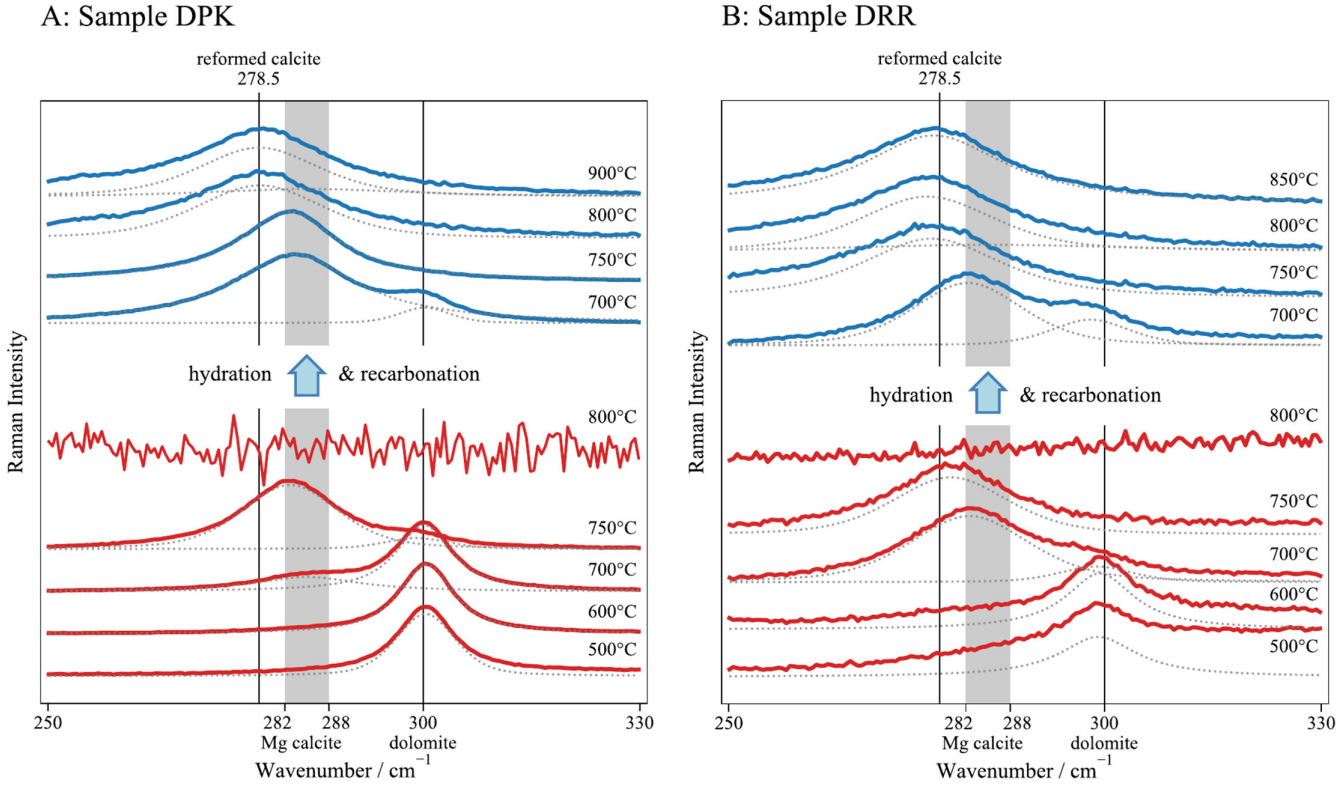

FIGURE 3 | Raman spectra of L-bands of carbonates measured at room temperature after calcination at different burning temperatures T_{burn} (red) and after subsequent hydration and recarbonation for 1 day (blue) for dolomite samples DPK (A) and DRR (B).

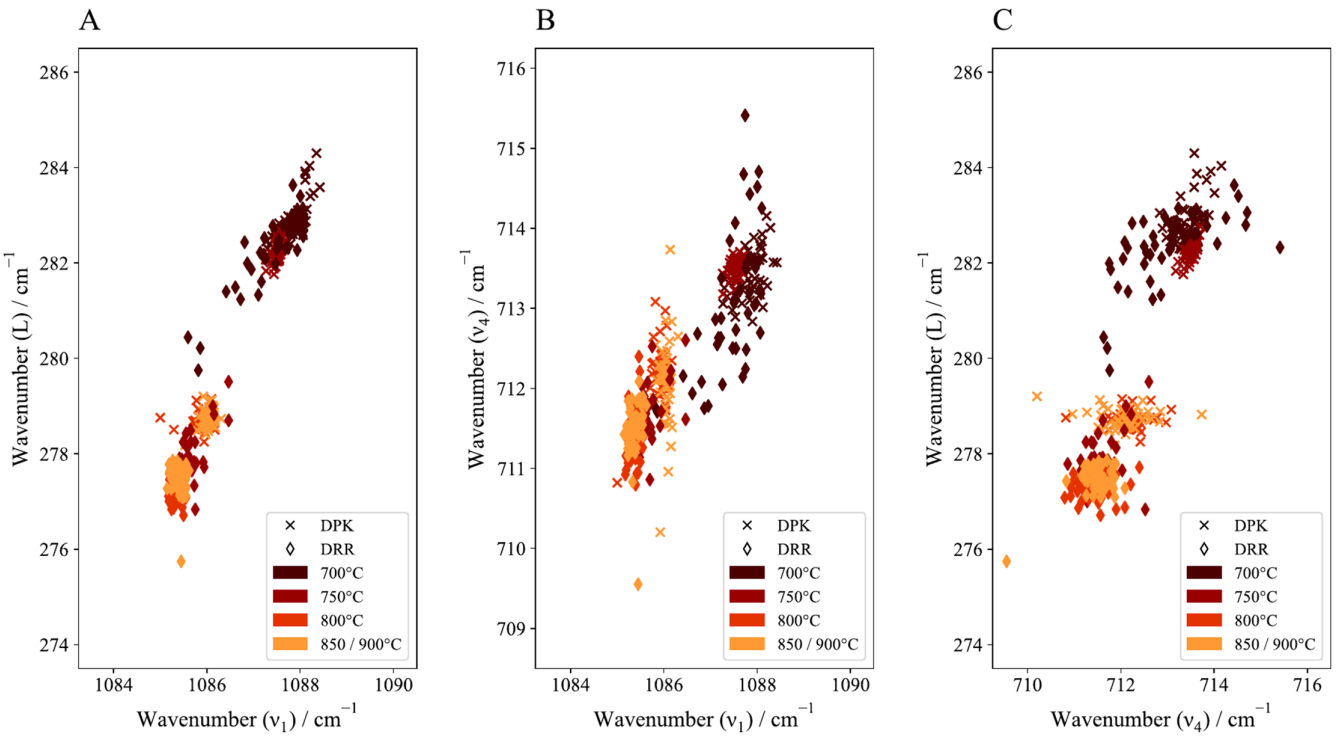

FIGURE 4 | Comparison of the peak position values of calcite in thermally treated dolomite samples after calcination at T_{burn} = 700°C–900°C, hydration, and recarbonation for 4 months: *L*- versus ν_1-mode (A); ν_4- versus ν_1-mode (B); *L*- versus ν_4-mode (C). n = 48 spectra for each sample at every T_{burn}.

Raman band parameters are achieved after the decarbonation, hydration, and recarbonation of dolomite.

After the discussed transformation, the central band peak positions remained stable even after four months of further carbonation in air with no significant changes of the peak positions. Raman signals suggesting the formation of brucite or Mg carbonate (hydrate) phases during this time span were not observed. Compared to CaO, MgO is less reactive and hydrates at slower rates [6, 8, 59]. The hydration of CaO to the more soluble Ca $(OH)_2$ further inhibits the hydration of MgO to the much less soluble Mg $(OH)_2$ [59, 60]. The relatively short slaking period before recarbonation likely contributed to formation of only trace amounts of brucite, leading to the absence of brucite bands in the spectra of the experimental samples. Further measurements aimed at resolving the more intense OH band around 3650 cm^{-1} may help identify brucite; however, this was not a priority for this study.

3.4 | Raman Microscopic Mapping of High-Fired Gypsum Mortar Sample

Figure 5 shows the results from Raman microscopic mapping of the high-fired gypsum mortar KeuperM, produced based on traditional manufacturing methods at Ziegelei Technisches Denkmal Hundisburg e.V. (Germany). An extended view of the microscopic image, peak fitting examples on the mortar sample, and histograms including mean values of the Raman band parameters are presented in Figures S5—9 in the Supporting Information.

Several polycrystalline, carbonatic fragments, and natural impurities of the gypsum deposit, were visible under the polarization microscope due to their high light refraction and birefringence (Figure 5A). The clusters vary in size, with diameters of a few hundred micrometers, each consisting of individual crystals ranging between 5 and 30 μm. Some of these agglomerates exhibited zoning with brownish coloring towards the edge. Raman microscopic mapping revealed a mixture of dolomite and calcium carbonate, with some carbonate grains also present in the surrounding gypsum matrix, along with thermal anhydrite (Figure 5B). Peak fitting of the anhydrite ν_1-mode revealed FWHM values mostly between 3.4 and 4.0 cm^{-1} (mean 3.8 ± 0.4 cm^{-1}, Figure 5C), indicating a burning temperature of 700°C–800°C according to our previous studies with pyrogenic anhydrite [17–20].

The Raman map in Figure 5B shows a simplified classification of each pixel to exactly one mineral. While many spectra consisted of several superimposed spectra of underlying minerals, in this assignment, an unambiguous classification was made and only the major component (i.e., the mineral with the strongest spectral contribution) was considered. Since most Raman spectra within the carbonate cluster showed a coexistence of dolomite and calcium carbonate, their respective ratio and their distribution within the carbonate cluster are of interest to potentially localize different stages of the dolomite decomposition and transformation to calcium carbonate. For this, the areas under the deconvolved dolomite ($A_{\nu1,\ dol}$) and calcium carbonate ν_1-bands ($A_{\nu1,\ cc}$) were used for an estimation of the relative amount of dolomite ($A_{rel,\ dol}$) in each Raman spectrum:

$$A_{rel,dol} = \frac{A_{\nu_1,dol}}{A_{\nu_1,dol} + A_{\nu_1,cc}} \quad (1)$$

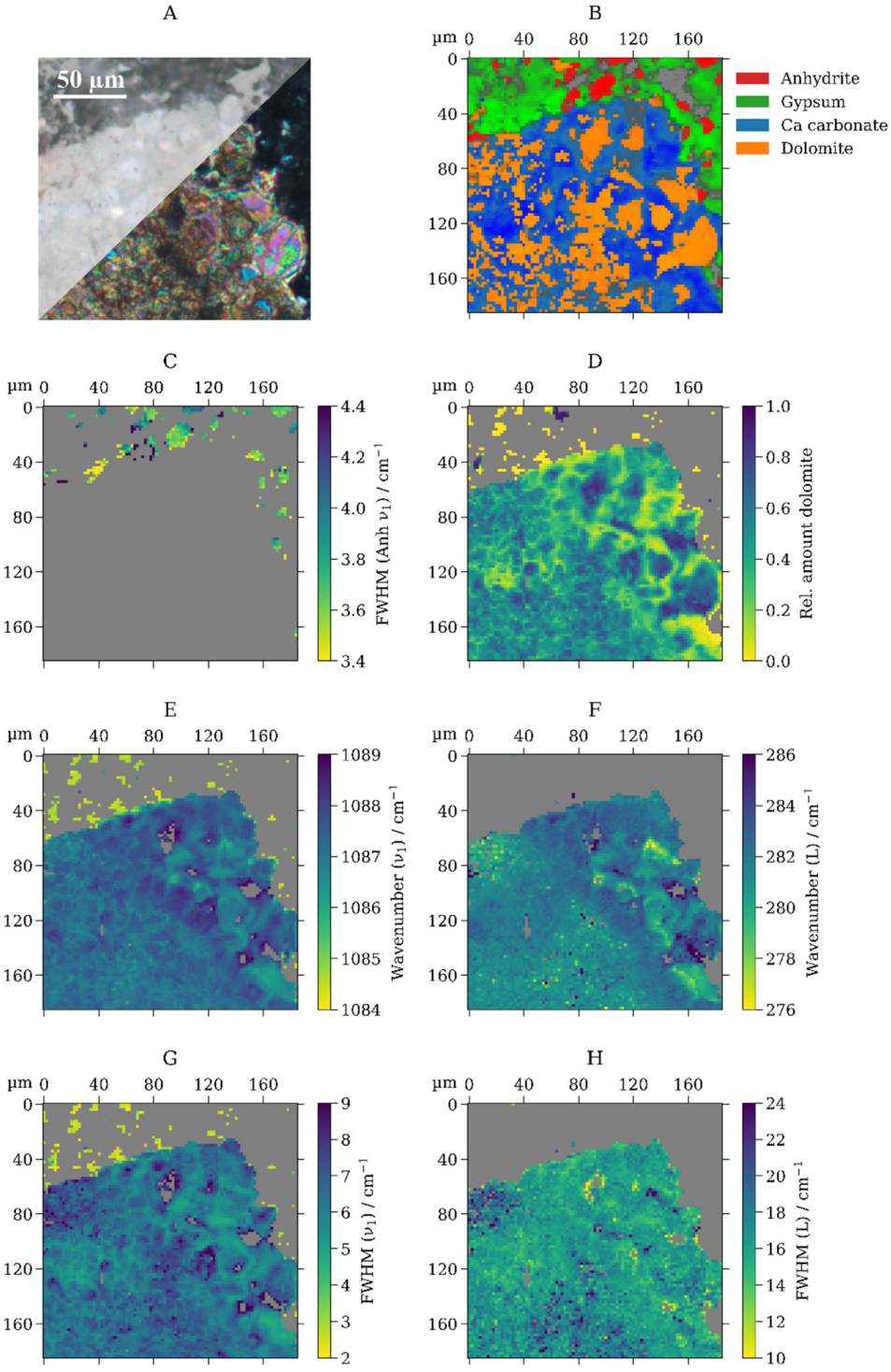

FIGURE 5 | Raman microscopy maps acquired on a thin-section sample of reenacted high-fired gypsum mortar KeuperM: Microscopic image, reflected light/transmitted light with crossed Nicols (A); Raman intensity distribution of marker bands for anhydrite (1017 cm^{-1}), gypsum (1008 cm^{-1}), calcium carbonate (1083–1090 cm^{-1}), dolomite (1098 cm^{-1}) (B); Raman band widths of anhydrite v_1-mode (C); relative amounts of dolomite calculated as the ratio of the integrals of the deconvoluted spectral contributions (0 = purely calcium carbonate, 1 = purely dolomite) (D); Raman peak positions of calcium carbonate v_1-mode (E) and *L*-mode (F); Raman band widths of calcium carbonate v_1-mode (G) and *L*-mode (H). Map sizes 94 × 94 px with 2 × 2 µm step size.

As seen in Figure 5D, this calculation also helped to better resolve the grain boundaries of the dolomite crystals within the carbonate cluster than with the intensity mapping in Figure 5B. The high contrast in the dolomite content showed that calcium carbonate occupies the areas between the dolomite islets. More extensive and continuous areas of calcium carbonate are found towards the rim compared to the core region of the cluster. These observations indicated a stronger degree of dolomite decomposition at the outer parts of the carbonate cluster, likely due to favorable energy and matter transport kinetics, such as

heat conductivity inside the samples or Mg diffusion out of the particles [6, 61].

Further insights into the degree of dolomite decomposition were obtained through the evaluation of the Raman peak positions and FWHM values of calcium carbonate (Figure 5E–H). Within the carbonate cluster, the peak positions of the ν_1-band varied between 1086 and 1089 cm^{-1} (mean 1087.2 ± 0.6 cm^{-1}), with few calcium carbonates found at 1085–1086 cm^{-1} (Figure 5E). The ν_1-FWHM values were mostly in the range of 5–8 cm^{-1} (mean 6.3 ± 1.0 cm^{-1}, Figure 5G). Similar contrast patterns showing the outlines of individual dolomite grains within the cluster were acquired in both peak position and FWHM maps. The calcium carbonate ν_1-bands exhibited higher peak positions at 1088–1089 cm^{-1} and larger FWHM values around 8–10 cm^{-1} in proximity to dolomite. Both values slightly decreased with decreasing dolomite content to 1086–1087 cm^{-1} and 5–7 cm^{-1}, respectively. The Raman maps of the calcium carbonate *L*-mode showed comparable contrast patterns as in the ν_1-mode maps (Figure 5F,H). The peak positions were mostly in the range of 280–283 cm^{-1} (mean 281.7 ± 1.2 cm^{-1}) and FWHM values were between 14 and 20 cm^{-1} (mean 16.6 ± 1.8 cm^{-1}). These results from the ν_1- and *L*-mode indicate that calcium carbonate within the cluster was predominantly Mg calcite, suggesting higher Mg concentration near dolomite sites. Where dolomite decomposition was more advanced, the Mg content in the calcites declined, resulting in a decrease in Raman peak positions.

Advanced calcination and reformation to Mg-free calcite was not evident, as Raman bands around 1086 cm^{-1} were found only sparsely in the Raman maps. However, calcium carbonates with lower ν_1-peak positions at 1084–1085 cm^{-1} (mean 1084.6 ± 0.3 cm^{-1}) and very low FWHM values around 2–3 cm^{-1} (mean 3.0 ± 1.0 cm^{-1}) were found at the most outer parts of the carbonate cluster and in the surrounding gypsum matrix (Figure 5E,G). These areas were also characterized by the absence of calcite *L*-bands around 275–286 cm^{-1} (Figure 5F). Instead, weaker Raman signals around 205 cm^{-1} indicated the presence of aragonite, the orthorhombic polymorph of calcium carbonate, at the outer areas. The aragonite found here was considered not of primary origin deriving from the raw material, as aragonite irreversibly transforms into calcite at 400–500 °C under ambient pressures [62, 63]. Aragonite has been reported in numerous studies after hydration and recarbonation of burned lime [22, 64, 65]. Different pathways for the nucleation of aragonite in lime binders have been summarized and discussed. In general, carbonation of $Ca(OH)_2$ completes with the formation of calcite, the most stable polymorph under room temperature and normal atmospheric pressure [22]. However, depending on the carbonation conditions, ACC, vaterite, and aragonite can form as metastable precursors during nucleation and growth of calcite [48, 50, 66]. The presence of Mg and SO_4 in aqueous solutions can strongly inhibit calcite crystallization and promote the nucleation of aragonite [67]. Considering that the Raman maps of KeuperM implied more advanced decomposition of dolomite to CaO and MgO at outer areas of the carbonate cluster, the aragonite found here likely formed in the high-Mg and high-SO_4 environment during the hydration and hardening process of the gypsum plaster. This may also explain the absence of Mg-free calcite with peak positions between 1085 and 1086 cm^{-1}, as CaO mostly reformed into aragonite.

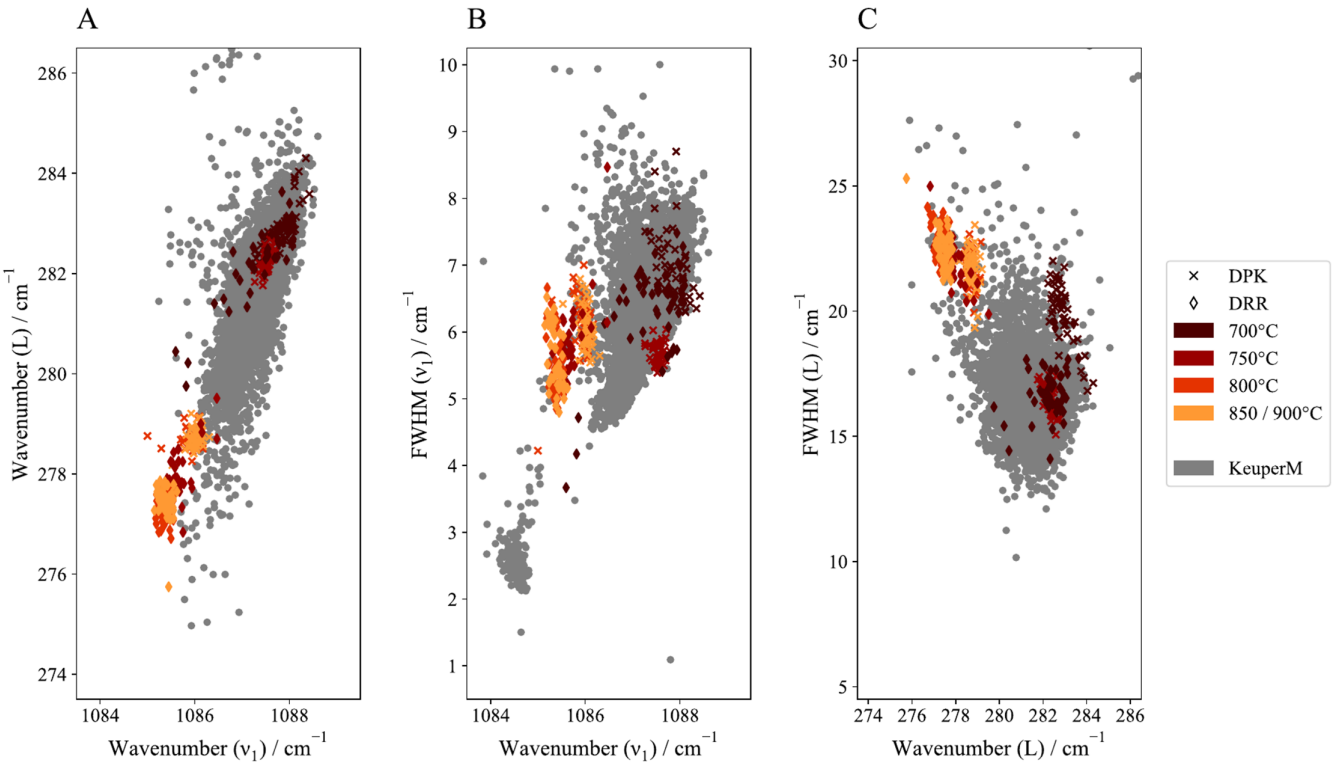

FIGURE 6 | Comparison of the Raman peak position and band width values of calcium carbonates in high-fired gypsum mortar KeuperM and thermally treated dolomite samples DPK and DRR (*n* = number of samples): Peak positions of *L*- versus ν_1-mode (A); band width versus peak positions of ν_1-mode (B); band width versus peak positions of *L*-mode (C). Values of thermally treated dolomite samples in (A) correspond to values in Figure 4A.

For further evaluation of the calcium carbonates in the KeuperM sample, the peak position and bandwidth values were compared to those of the recarbonated samples from the thermal experiments with dolomite, as shown in Figure 6. A more comprehensive comparison, including Raman data of various untreated, geogenic carbonate samples, is provided in the Supporting Information (Table S1 and Figure S10). Most calcium carbonate spectra from the KeuperM sample overlapped with the Mg calcite spectra of the experimental samples treated at 700°C–750°C. These spectra exhibited higher peak positions for the ν_1- and L-mode (Figure 6A), higher FWHM values of the ν_1-band between 5 and 9 cm^{-1} (Figure 6B), and moderately high FWHM values of the L-band around 15–20 cm^{-1} (Figure 6C). This overlap, along with the estimation of the burning temperature using pyrogenic anhydrite, aligns well with previous temperature measurements at Ziegelei Hundisburg. Schlütter et al. reported a gradual increase in kiln temperature to approx. 800°C in the center of the kiln after 11 h, with further firing at this temperature for another 2 h [68]. Due to differences in grain sizes of the raw material and local temperature gradients, various stages of the transformation process were preserved in the carbonate aggregate: intact dolomite, partially decomposed to Mg calcite, and traces of complete decomposition and recarbonation to aragonite at the rim.

4 | Conclusion

The thermal decomposition of two natural dolomite samples was examined with high-spectral resolution Raman spectroscopy. For both samples, the decarbonation comprised a first calcination step at T_{burn} = 700°C–750°C, where Mg calcite was found as the principal product (MgO is Raman silent). Upon higher temperatures, Mg calcite further stoichiometrically decomposes to CaO in a second calcination step above 800°C and reforms to Mg-free calcite upon hydration and recarbonation in air. While the spectral width of the observed Raman bands reflects the micro-homogeneity of the sample, the incorporation of Mg in the crystal lattice of calcite decreases the interatomic distances, which results in a proportional increase of the Raman shifts of all vibrational modes of calcite. Hence, Raman peak position and bandwidth analysis allow the spectroscopic discrimination between pyrogenic Mg calcites formed at different calcination temperatures. Raman microspectroscopic mapping on thin sections of a reenacted high-fired gypsum mortar confirmed the presence of Mg calcite in association with thermally stressed dolomitic impurities. Comparison of the Raman band parameters of the calcium carbonates showed high similarity with Mg calcite formed at T_{burn} = 700°C–750°C in the experimental samples, matching well with the burning regime reported by the manufacturer Ziegelei Hundisburg and the calculated temperature estimation based on thermal anhydrite grains in the binder matrix. Thus, the Raman spectroscopic study of pyrogenic Mg calcites represents a complementary approach to the analysis of pyrogenic anhydrite for the determination of the burning temperature of high-fired gypsum mortars. These findings yet again highlight the potential of high-spectral resolution Raman microspectroscopy for the thermometric analysis of (anthropogenic) fired materials. Further research should focus on the influence of other preparatory parameters on the Raman bands of the products of the thermal breakdown of dolomite, e.g., grain size distribution of the raw material, prolonged calcination and hydration periods, and carbonation conditions. Furthermore, the applicability of this method on underburned dolomite grains in other building materials, such as dolomitic lime mortars, and ceramics, remains to be tested. Including high-spectral resolution Raman microspectroscopy into future studies can thus not only help elucidating the thermal history of fired materials in archaeology and art technology to deepen our understanding of the lost medieval production technology, but also be beneficial for quality controls in the present production of mineral binders.

Acknowledgments

We gratefully acknowledge funding of this research by the Deutsche Forschungsgemeinschaft DFG (Project no. 458702855) and the Interreg VI-A Italy-Austria program 2021-2027 (Project no. ITAT-11-027 SaltAR). We thank the School of Analytical Sciences Adlershof (SALSA) for providing laboratory space and equipment. Furthermore, we thank Gerd Srocke (Architekturbüro Gerd Srocke, expert advisor Technisches Denkmal Ziegelei Hundisburg e.V.) for providing high-fired gypsum mortar samples, Dr. Ralf-Thomas Schmitt (Museum für Naturkunde Berlin) for providing dolomite samples, Christine Fischer (Institute of Geosciences, University of Potsdam) for sample preparation, and Dr. Markus Ostermann (BAM division 1.4) for XRF measurements. Open Access funding enabled and organized by Projekt DEAL.

Conflicts of Interest

The authors declare no conflicts of interest.

Data Availability Statement

The data that support the findings of this study are available from the corresponding author upon reasonable request.

References

1. C. Rodriguez-Navarro, K. Kudlacz, and E. Ruiz-Agudo, "The Mechanism of Thermal Decomposition of Dolomite: New Insights From 2D-XRD and TEM Analyses," *American Mineralogist* 97 (2012): 38–51.

2. L. C. Resio, "Dolomite Thermal Behaviour: A Proposal to Establish a Definitive Decomposition Mechanism in a Convective Air Atmosphere," *Open Ceramics* 15 (2023): 100405.

3. K. V. Balen, in *Proceedings of the First International Congress on Construction History*, vol. 3 (2003): 2041–2054.

4. J. I. Alvarez, R. Veiga, S. Martínez-Ramírez, et al., "RILEM TC 277-LHS Report: A Review on the Mechanisms of Setting and Hardening of Lime-Based Binding Systems," *Materials and Structures* 54 (2021): 63.

5. J. Elsen, M. D. Jackson, and E. Ruiz-Agudo, "Historic Concrete Science:Opus Caementiciumto "Natural Cements"," *Elements* 18 (2022): 301–307.

6. H. Siedel, S. Michalski, and H.-W. Zier, *Umweltbedingte Gebäudeschäden an Denkmälern durch die Verwendung von Dolomitkalkmörteln*, vol. 16 (Institut für Steinkonservierung e.V, 2003): 7–11.

7. A. Diekamp, J. Konzett, and M. Peter, in *Proceedings of the 12th Euroseminar on Microscopy Applied to Building Materials (EMABM)*, (2009): 309–317.

8. A. Diekamp, Bindemitteluntersuchungen an historischen Putzen und Mörteln aus Tirol und Südtirol, Dissertation, Leopold-Franzens-Universität Innsbruck, 2014.

9. A. Diekamp, *Alles Kalk! Wissenschaftliches Kolloquium zu Kalkmörteln, −putzen und -farben anlässlich des 30-jährigen Bestehens des Instituts für Steinkonservierung e.V*, vol. 62 (Institut für Steinkonservierung e.V, 2021): 81–96.

10. T. Schmid and P. Dariz, "Determination and Imaging of Binder Remnants and Aggregates in Historic Cement Stone by Raman Microscopy," *Journal of Raman Specroscopy* 44 (2013): 882–891.

11. T. Schmid and P. Dariz, "Chemical Imaging of Historical Mortars by Raman Microscopy," *Construction and Building Materials* 114 (2016): 506–516.

12. K. Stange, C. Lenting, and T. Geisler, "Insights Into the Evolution of Carbonate-Bearing Kaolin During Sintering Revealed by In Situ Hyperspectral Raman Imaging," *Journal of the American Ceramic Society* 101 (2018): 897–910.

13. K. Hauke, J. Kehren, N. Böhme, S. Zimmer, and T. Geisler, "In Situ Hyperspectral Raman Imaging: A New Method to Investigate Sintering Processes of Ceramic Material at High-Temperature," *Applied Sciences* 9 (2019): 1310.

14. N. Böhme, K. Hauke, M. Neuroth, and T. Geisler, "In Situ Hyperspectral Raman Imaging of Ternesite Formation and Decomposition at High Temperatures," *Minerals* 10 (2020): 287.

15. K. C. Polavaram and N. Garg, "Enabling Phase Quantification of Anhydrous Cements via Raman Imaging," *Cement and Concrete Research* 150 (2021): 106592.

16. P. Dariz, C. Jakob, D. Ectors, J. Neubauer, and T. Schmid, "Measuring the Burning Temperatures of Anhydrite Micrograins in a High-Fired Medieval Gypsum Mortar," *ChemistrySelect* 2 (2017): 9153–9156.

17. T. Schmid, R. Jungnickel, and P. Dariz, "Raman Band Widths of Anhydrite II Reveal the Burning History of High-Fired Medieval Gypsum Mortars," *Journal of Raman Specroscopy* 50 (2019): 1154–1168.

18. T. Schmid and P. Dariz, "Raman Microspectroscopic Imaging of Binder Remnants in Historical Mortars Reveals Processing Conditions," *Heritage* 2 (2019): 1662–1683.

19. P. Dariz and T. Schmid, "Phase Composition and Burning History of High-Fired Medieval Gypsum Mortars Studied by Raman Microspectroscopy," *Materials Characterization* 151 (2019): 292–301.

20. T. Schmid, R. Jungnickel, and P. Dariz, "Insights into the CaSO4–H2O System: A Raman-Spectroscopic Study," *Minerals* 10 (2020): 115.

21. P. Dariz, U. G. Wortmann, J. Vogl, and T. Schmid, "Beautiful Pietàs in South Tyrol (Northern Italy): Local or Imported Works of Art?," *Heritage Science* 10 (2022): 10.

22. S. Martinez-Ramirez, S. Sanchez-Cortes, J. V. Garcia-Ramos, C. Domingo, C. Fortes, and M. T. Blanco-Varela, "Micro-Raman Spectroscopy Applied to Depth Profiles of Carbonates Formed in Lime Mortar," *Cement and Concrete Research* 33 (2003): 2063.

23. R. Ševčík, P. Mácová, K. Sotiriadis, M. Pérez-Estébanez, A. Viani, and P. Šašek, "Micro-Raman Spectroscopy Investigation of the Carbonation Reaction in a Lime Paste Produced With a Traditional Technology," *Journal of Raman Specroscopy* 47 (2016): 1452–1457.

24. S. Hild, O. Marti, and A. Ziegler, "Spatial Distribution of Calcite and Amorphous Calcium Carbonate in the Cuticle of the Terrestrial Crustaceans *Porcellio scab*er and *Armadillidium vulgare*," *Journal of Structural Biology* 163 (2008): 100–108.

25. U. Wehrmeister, D. E. Jacob, A. L. Soldati, N. Loges, T. Häger, and W. Hofmeister, "Amorphous, Nanocrystalline and Crystalline Calcium Carbonates in Biological Materials," *Journal of Raman Specroscopy* 42 (2011): 926–935.

26. A. Badou, S. Pont, S. Auzoux-Bordenave, M. Lebreton, and J.-F. Bardeau, "New Insight on Spatial Localization and Microstructures of Calcite-Aragonite Interfaces in Adult Shell of *Haliotis tuberculata*: Investigations of Wild and Farmed Abalones by FTIR and Raman Mapping," *Journal of Structural Biology* 214 (2022): 107854.

27. S. Calandra, C. Conti, I. Centauro, and E. Cantisani, "Non-Destructive Distinction Between Geogenic and Anthropogenic Calcite by Raman Spectroscopy Combined with Machine Learning Workflow," *Analyst* 148 (2023): 2861–2870.

28. M. B. Toffolo, I. Pinkas, A. Á. Gallo, and E. Boaretto, "Crystallinity Assessment of Anthropogenic Calcites Using Raman Micro-Spectroscopy," *Scientific Reports* 13 (2023): 12971.

29. S. Gunasekaran and G. Anbalagan, "Spectroscopic Study of Phase Transitions in Dolomite Mineral," *Journal of Raman Specroscopy* 38 (2007): 846–852.

30. S. Gunasekaran and G. Anbalagan, "Thermal Decomposition of Natural Dolomite," *Bulletin of Materials Science* 30 (2007): 339–344.

31. N. Oriols, N. Salvadó, T. Pradell, et al., "Carbonation of Fresco Mural Paintings With a Dolomitic Mortar," *Cement and Concrete Research* 157 (2022): 106828.

32. K. P. G. and C. KG, Dolomit, rein weiß, 10 µ Füllstoffe & Baustoffe, https://www.kremer-pigmente.com/de/shop/fuellstoffe-baustoffe/58740-dolomit-rein-weiss-10-u.html, (accessed 30 August 2024).

33. Hochbrandgips – Technisches Denkmal Ziegelei Hundisburg, https://www.ziegelei-hundisburg.de/hochbrandgips, (accessed 30 August 2024).

34. R. W. Berg and T. Nørbygaard, "Wavenumber Calibration of CCD Detector Raman Spectrometers Controlled by a Sinus Arm Drive," *Applied Spectroscopy Reviews* 41 (2006): 165.

35. R. J. Bakker, "The Perfection of Raman Spectroscopic Gas Densimeters," *Journal of Raman Specroscopy* 2021 (1923): 52–1948.

36. X. Yuan and R. A. Mayanovic, "An Empirical Study on Raman Peak Fitting and Its Application to Raman Quantitative Research," *Applied Spectroscopy* 71 (2017): 2325–2338.

37. M. Newville, R. Otten, A. Nelson, et al., *LMFIT: Non-linear Least-Squares Minimization and Curve-Fitting for Python* (Zenodo, 2025), https://doi.org/10.5281/zenodo.15014437.

38. W. D. Bischoff, S. K. Sharma, and F. T. MacKenzie, "Carbonate Ion Disorder in Synthetic and Biogenic Magnesian Calcites: A Raman Spectral Study," *American Mineralogist* 70 (1985): 581.

39. L. Borromeo, U. Zimmermann, S. Andò, et al., "Raman Spectroscopy as a Tool for Magnesium Estimation in Mg-Calcite," *Journal of Raman Specroscopy* 48 (2017): 983–992.

40. N. Rividi, M. Zuilen, P. Philippot, B. Ménez, G. Gaston, and E. Poidatz, "Calibration of Carbonate Composition Using Micro-Raman Analysis: Application to Planetary Surface Exploration," *Astrobiology* 10 (2010): 293.

41. D. Wang, L. M. Hamm, R. J. Bodnar, and P. M. Dove, "Raman Spectroscopic Characterization of the Magnesium Content in Amorphous Calcium Carbonates," *Journal of Raman Specroscopy* 43 (2012): 543–548.

42. D. Krishnamurti, "Raman Spectrum of Magnesite," *Proceedings of the Indian Academy of Sciences—Section A* 43 (1956): 210.

43. J. Sun, Z. Wu, H. Cheng, Z. Zhang, and R. L. Frost, "A Raman Spectroscopic Comparison of Calcite and Dolomite," *Spectrochimica Acta. Part A, Molecular and Biomolecular Spectroscopy* 117 (2014): 158.

44. T. Schmid and P. Dariz, "Shedding Light Onto the Spectra of Lime: Raman and Luminescence Bands of CaO, Ca(OH)2and CaCO3," *Journal of Raman Specroscopy* 46 (2015): 141–146.

45. T. Schmid, R. Kraft, and P. Dariz, "Shedding Light Onto the Spectra of Lime—Part 2: Raman Spectra of Ca and Mg Carbonates and the Role of d-Block Element Luminescence," *Journal of Raman Specroscopy* 52 (2021): 1462–1472.

46. M. Dekermenjian, A. P. Ruediger, and A. Merlen, "Raman Spectroscopy Investigation of Magnesium Oxide Nanoparticles," *RSC Advances* 13 (2023): 26683–26689.

47. L. Black, *Spectroscopic Properties of Inorganic and Organometallic Compounds*, vol. 40, eds. J. Yarwood, R. Douthwaite, and S. Duckett (Royal Society of Chemistry, 2009): 72–127.

48. Ö. Cizer, C. Rodriguez-Navarro, E. Ruiz-Agudo, J. Elsen, D. Van Gemert, and K. Van Balen, "Phase and Morphology Evolution of Calcium Carbonate Precipitated by Carbonation of Hydrated Lime," *Journal of Materials Science* 47 (2012): 6151–6165.

49. E. Dubina, L. Korat, L. Black, J. Strupi-Suput, and J. Plank, "Influence of Water Vapour and Carbon Dioxide on Free Lime During Storage at 80°C, Studied by Raman Spectroscopy," *Spectrochimica Acta Part A: Molecular and Biomolecular Spectroscopy* 111 (2013): 299–303.

50. C. Rodriguez-Navarro, K. Elert, and R. Ševčík, "Amorphous and Crystalline Calcium Carbonate Phases During Carbonation of Nanolimes: Implications in Heritage Conservation," *CrystEngComm* 18 (2016): 6594–6607.

51. E. Loste, R. M. Wilson, R. Seshadri, and F. C. Meldrum, "The Role of Magnesium in Stabilising Amorphous Calcium Carbonate and Controlling Calcite Morphologies," *Journal of Crystal Growth* 254 (2003): 206–218.

52. B. Purgstaller, V. Mavromatis, A. Immenhauser, and M. Dietzel, "Transformation of Mg-Bearing Amorphous Calcium Carbonate to Mg-Calcite—In Situ Monitoring," *Geochimica et Cosmochimica Acta* 174 (2016): 180–195.

53. F. Konrad, B. Purgstaller, F. Gallien, V. Mavromatis, P. Gane, and M. Dietzel, "Influence of Aqueous Mg Concentration on the Transformation of Amorphous Calcium Carbonate," *Journal of Crystal Growth* 498 (2018): 381–390.

54. P. G. Caceres and E. K. Attiogbe, "Thermal Decomposition of Dolomite and the Extraction of Its Constituents," *Minerals Engineering* 10 (1997): 1165–1176.

55. É. Kristóf-Makó and A. Z. Juhász, "The Effect of Mechanical Treatment on the Crystal Structure and Thermal Decomposition of Dolomite," *Thermochimica Acta* 342 (1999): 105–114.

56. R. M. McIntosh, J. H. Sharp, and F. W. Wilburn, "The Thermal Decomposition of Dolomite," *Thermochimica Acta* 165 (1990): 281.

57. H.-G. Wiedemann and G. Bayer, "Note on the Thermal Decomposition of Dolomite," *Thermochimica Acta* 121 (1987): 479–485.

58. J. M. Valverde, A. Perejon, S. Medina, and L. A. Perez-Maqueda, "Thermal Decomposition of Dolomite Under CO2: Insights From TGA and In Situ XRD Analysis," *Physical Chemistry Chemical Physics* 17 (2015): 30162–30176.

59. D. R. Glasson, "Reactivity of Lime and Related Oxides. XII. Hydration of Dolomitic Lime," *Journal of Applied Chemistry* 14 (1964): 125–128.

60. S. Ruan and C. Unluer, "Comparison of the Environmental Impacts of Reactive Magnesia and Calcined Dolomite and Their Performance under Different Curing Conditions," *Journal of Materials in Civil Engineering* 30 (2018): 04018279, https://doi.org/10.1061/(ASCE)MT.1943-5533.0002471.

61. H. Galai, M. Pijolat, K. Nahdi, and M. Trabelsi-Ayadi, "Mechanism of Growth of MgO and $CaCO_3$ During a Dolomite Partial Decomposition," *Solid State Ionics* 178 (2007): 1039.

62. S. Yoshioka and Y. Kitano, "Transformation of Aragonite to Calcite Through Heating," *Geochemical Journal* 19 (1985): 245.

63. S. M. Antao and I. Hassan, "Temperature Dependence of the Structural Parameters in the Transformation of Aragonite to Calcite, as Determined from In Situ Synchrotron Powder X-Ray-Diffraction Data," *Canadian Mineralogist* 48 (2010): 1225–1236.

64. M. B. Toffolo and E. Boaretto, "Nucleation of Aragonite Upon Carbonation of Calcium Oxide and Calcium Hydroxide at Ambient Temperatures and Pressures: A New Indicator of Fire-Related Human Activities," *Journal of Archaeological Science* 49 (2014): 237–248.

65. M. B. Toffolo, "The Significance of Aragonite in the Interpretation of the Microscopic Archaeological Record," *Geoarchaeology* 36 (2021): 149–169.

66. G. Montes-Hernandez and F. Renard, "Time-Resolved in Situ Raman Spectroscopy of the Nucleation and Growth of Siderite, Magnesite, and Calcite and Their Precursors," *Crystal Growth & Design* 16 (2016): 7218–7230.

67. K. E. Goetschl, B. Purgstaller, M. Dietzel, and V. Mavromatis, "Effect of Sulfate on Magnesium Incorporation in Low-Magnesium Calcite," *Geochimica et Cosmochimica Acta* 265 (2019): 505–519.

68. F. Schlütter, W. Kaiser, and H. Juling, in *Proceedings of the 2nd Historic Mortars Conference HMC2010 and RILEM TC 203-RHM Final Workshop* (2010): 1169–1180.

Supporting Information

Additional supporting information can be found online in the Supporting Information section.